

Disorder-induced electron and hole trapping in amorphous TiO₂David Mora-Fonz ^{1,*}, Moloud Kaviani ² and Alexander L. Shluger ¹¹*Department of Physics and Astronomy, University College London, Gower Street, London WC1E 6BT, United Kingdom*²*Department of Chemistry and Biochemistry, University of Bern, Freiestrasse 3, CH-3012 Bern, Switzerland*

(Received 22 May 2020; accepted 23 July 2020; published 13 August 2020)

Thin films of amorphous (a)-TiO₂ are ubiquitous as photocatalysts, protective coatings, photo-anodes, and in memory applications, where they are exposed to excess electrons and holes. We investigate trapping of excess electrons and holes in the bulk of pure amorphous titanium dioxide, a-TiO₂, using hybrid density-functional theory (h-DFT) calculations. Fifty 270-atom a-TiO₂ structures were produced using classical molecular dynamics and their geometries fully optimized using h-DFT simulations. They have the density, distribution of atomic coordination numbers, and radial pair-distribution functions in agreement with experiments. The calculated average a-TiO₂ band gap is 3.25 eV with no states splitting into the band gap. Trapping of excess electrons and holes in a-TiO₂ is predicted at precursor sites, such as elongated Ti–O bonds. Single electron and hole polarons have average trapping energies (E_T) of -0.4 eV and -0.8 eV, respectively. We also identify several types of electron and hole bipolaron states and discuss their stability. These results can be used for understanding the mechanisms of photo-catalysis and improving the performance of electronic devices employing a-TiO₂ films.

DOI: [10.1103/PhysRevB.102.054205](https://doi.org/10.1103/PhysRevB.102.054205)**I. INTRODUCTION**

TiO₂-based materials and devices are studied extensively due to their optical, dielectric, catalytic, thermal, and mechanical properties (see, e.g., Refs. [1–4] and references therein). In technological applications, these materials are often produced as thin films or powders by employing various techniques, such as atomic layer deposition, chemical vapor deposition, electron beam deposition, reactive evaporation, plasma plating, sputtering, and others [5,6]. The initially grown TiO₂ films and nanoparticles are amorphous or polycrystalline [7] and undergo further thermal treatment to achieve desired technological properties. Amorphous TiO₂ films are used as protective coatings for concentrated solar power mirrors [8], photoanodes [9], and in nonvolatile memory applications [10].

The performance of these as well as other systems used in photocatalysis and photoelectrocatalysis [11] is affected or governed by electrons and/or holes induced by dopants (such as H, Li, Nb, and vacancy defects) [12–17], photoexcitation, and as a result of carrier injection from electrodes. In similar wide-gap semiconductors, excess charges often localize at regular lattice sites or impurities and modify the electronic structure by creating the corresponding shallow or deep gap states [18]. These localized states may degrade the electronic properties of the material or provide opportunities for band-gap engineering. For example, electron and hole localization reduces electrical and photo-conductivity of materials. In contrast, electron–hole recombination is highly undesirable, leading to short exciton lifetimes and a poor photocatalyst. Therefore, it is important to understand how excess carriers interact with materials.

Small polarons in the two main TiO₂ polymorphs, rutile and anatase, have been studied experimentally [16,19–22] and theoretically using density-functional theory (DFT)-based methods [23–34] and their properties have recently been reviewed in, e.g., Refs. [32,35,36] and references therein. In rutile, there is a general agreement that self-trapped electron polarons are stable: Experiments report a much slower electron polaron transport (with thermal activation energies around -20 and -30 meV) [19] than a bandlike conduction, which is an indication of the preference for localized electrons. At the same time, calculations predict exothermic trapping energies, E_T , ranging from -0.02 to -0.4 eV [29,32,35]. For self-trapped holes in rutile, opinions are divided, with electron paramagnetic resonance measurements suggesting either the formation [37] or no formation of hole traps [21]. Similarly, DFT (DFT+ U , DFT + polaron correction [35]) and h-DFT calculations (HSE06, PBE0-TC-LRC [32]) predict exothermic and endothermic holes E_T , respectively. In anatase, both experiment and theory agree that holes are trapped in deep hole polaron states, but electron polarons are metastable. The experimental evidence shows that the hole trapping in anatase is deeper and more localized than the electron trapping in rutile [38].

In spite of wide applications, relatively little is still known regarding intrinsic electron and hole trapping in a-TiO₂. The structure and electronic properties of stoichiometric and reduced a-TiO₂ have been modeled using a combination of classical structure simulations and DFT-based calculations [39–43]. DFT+ U calculations [39] of a single amorphous structure predicted stable hole E_T (-1.3 eV) at intrinsic sites in a-TiO₂, in contrast to rutile, where the endothermic E_T ($+0.5$ eV) has been calculated. In addition, trapping of electrons has been observed in the bulk of a-TiO₂ nanoparticles [44] and electron trapping in-

*david.fonz.11@ucl.ac.uk

duced by Fe impurities in a-TiO₂ has been calculated using DFT+*U* [45].

Deep electron and hole trapping has been predicted in several other amorphous oxides where polarons do not trap or form only shallow states in crystalline phase [46]. In particular, theoretical studies have shown that the precursor sites composed of wide O–Si–O bond angles act as deep electron traps in amorphous SiO₂ [47]. These sites can accommodate up to two extra electrons [48]. In amorphous InGaZnO₄ [49] and HfO₂ [50], undercoordinated indium and hafnium atoms, respectively, are shown to serve as precursors for the deep electron trapping. Similar precursors also act as electron traps at surfaces and grain boundaries [51–55]. Holes have been shown to trap at low-coordinated oxygen sites in most amorphous oxides, including ZnO, Al₂O₃, HfO₂ and SiO₂. [46,56].

The fact that disorder can produce precursor sites for formation of deep localized electron and hole states suggests that balance between the short-ranged phonon-mediated attraction and on-site Hubbard repulsion could be tipped in favor of formation of bipolaronlike states where two electrons or holes coexist on one or several neighboring network sites. The possibility of formation of such states in crystals [57,58] and amorphous solids [59,60] has been predicted by the phenomenological theory and demonstrated in some oxides by DFT simulations [46]. Electron bipolarons have been predicted by DFT calculations in amorphous SiO₂ [48] and HfO₂ [50]. Hole bipolarons have been predicted in both crystalline (e.g., BiVO₄ [61], V₂O₅, TiO₂ [62]) and amorphous oxides (Al₂O₃, HfO₂ [63]). The formation of hole bipolaron states is associated with the formation of peroxidelike O–O states inside the oxide [62,63].

Here, we study the electronic structure and electron- and hole-trapping properties of a-TiO₂ using a h-DFT approach, which has been carefully calibrated to model polarons in six different phases of TiO₂ in Ref. [32]. Fifty 270-atom structures were used to obtain the distribution of structural and electronic properties, including their inverse participation ratio (IPR) spectrum, of a-TiO₂. Every structure was tested for electron and hole trapping. We demonstrate that Ti and O ions serve as precursor sites for deep electron and hole trapping in a-TiO₂ with an average E_T of about -0.8 eV and -0.4 eV for holes and electrons, respectively. We also identify several types of electron and hole bipolaron-type states and discuss their stability. These results may have important implications for applications for understanding the properties and performance of (photo)catalysis, electronics, memory devices, and batteries.

II. COMPUTATIONAL DETAILS

The structure of a-TiO₂ has been studied experimentally in Refs. [7,65,66]. Following the success in experimental preparation of metastable metal alloys [67], theoretical models of oxide glasses are also usually obtained using a melt-quench procedure and molecular dynamics (MD) [68]. This technique has been used to model structures of amorphous a-HfO₂, a-SiO₂, a-Al₂O₃, a-ZnO, and a-Sm₂O₃ [47,50,56,69–71] as well as other non-glass-forming oxides [72]. Similarly, classical force-fields, [39,73–80] density-functional-based tight-

binding [81] and DFT [41–43,64] simulations have been used to create models of a-TiO₂ structures.

We employed classical force-field MD simulations followed by a complete structural relaxation of obtained structures using h-DFT. We used the LAMMPS package [82] with the Matsui-Akaogi force field [73], which has been shown to reproduce the structural properties of the crystalline, liquid, and amorphous phases of TiO₂ with accuracy close to first-principles methods [41,81]. We have indeed shown the success of IPs in reproducing physical and structural properties with high accuracy for different materials, including TiSe₂, [83] In₂O₃-SnO₂, [84] ZnO, [85] among others. To study the distribution of properties of trapped carriers in a-TiO₂, we created 50 different amorphous structures using MD at constant pressure and a Nosé-Hoover thermostat and barostat. As the initial structure, in all cases, we used a cubic periodic cell containing 270 atoms distributed randomly across the simulation cell. First, the structures were equilibrated at 300 K for 50 ps and then the temperature was linearly increased to 5000 K for 50 ps. The melt was further equilibrated for 500 ps at 5000 K. The systems were cooled down from 5000 K to 300 K during 4.7 ns with a cooling rate of 1 K ps⁻¹. Finally, the structures were equilibrated for 50 ps at 300 K. We note that the initial structure has no effect on the topology of our amorphous structures due to the long-time simulation of the melt.

Further optimization of the geometry and volume of these structures along with the subsequent electronic structure calculations were performed using DFT as implemented in the CP2K code [86,87]. CP2K employs a Gaussian basis set mixed with an auxiliary plane-wave-basis set [88]. The double- and triple- ζ Gaussian basis sets [89] were employed on oxygen and titanium atoms in conjunction with the Goedecker-Teter-Hutter (GTH) pseudopotential [90]. The plane-wave cutoff was set to 8163 eV (600 Ry), which is sufficient to converge the *r*-TiO₂ bulk lattice energy (six atoms) to less than 1 meV. To avoid the bond-length overestimation typical for generalized gradient approximation (GGA) functionals, for preliminary geometry optimization we used the PBEsol functional [91], which is a flavor of the well-known PBE functional [92] and is known to produce lattice parameters in solids with relatively higher accuracy. This gives a better starting point for the subsequent more expensive hybrid functional calculations.

Accurate prediction of polaron states is challenging due to the self-interaction error inherent in DFT [93–96]. It is widely accepted that hybrid functionals can reliably describe properties of insulators and currently present the best choice to accurately describe localized electron and hole states. The obtained amorphous structures have been further fully optimized with the hybrid PBE0-TC-LRC functional [87]. This truncated-Coulomb long-range corrected version of the hybrid functional PBE0 is known to provide accurate band gaps and structural properties of insulators and is of similar form as the hybrid HSE06 functional [97] but is less computationally demanding. This is achieved by truncating the computation of the exact exchange by cutoff radius (R_c). The amount of exact exchange and its cutoff radius can be adjusted to achieve optimum accuracy for a particular system. In this paper, we use a cutoff radius $R_c = 6$ Å and the amount of exact exchange $\alpha = 0.115$, which have recently been optimized

TABLE I. Bulk properties of the rutile and anatase structure of TiO₂.

	Rutile		Anatase	
	This paper	Expt.	This paper	Expt.
a (Å)	4.615	4.587	3.788	3.782
c (Å)	2.960	2.954	9.626	9.502
Band gap (eV)	2.80	3.0	3.02	3.2
E_T (h ⁺ , eV)			0.25	
E_T (e ⁻ , eV)	0.02			

[32] to model polaron formation in six different TiO₂ crystal structures, including rutile, anatase, and brookite. Employing these parameters, one obtains structural parameters of crystalline TiO₂ in agreement with experiments, a band gap within 6% from experimental values for anatase and rutile, and satisfies the generalized Koopmans' condition (gKc) to within 0.08 eV for all six different TiO₂ phases. The latter is important to provide an accurate prediction of small polarons across all TiO₂ phases [32]. To reduce the computational cost of nonlocal functional calculations, the auxiliary density matrix method was employed [98]. All geometry optimizations were performed using the Broyden-Fletcher-Goldfarb-Shanno (BFGS) optimizer to minimize forces on atoms to within 0.02 eV Å⁻¹. All calculations are performed at the Γ point.

The electron/hole trapping energy, E_T , a measure of stability of localized states, is calculated as the difference between total energies of the delocalized and fully localized electron states. We note that distribution of calculated E_T is affected by several factors compared to similar calculations in the crystal phase, as discussed in detail in Ref. [56]. One of the major factors is the partially localized character of the initial state, which is discussed below along with the other aspects. As a comparison, ten a-TiO₂ structures were fully reoptimized and their E_T calculated using the hybrid HSE06 functional, which has been widely used to study defects and polarons in TiO₂.

All crystal structures in this paper were generated using the VESTA package [99] whereas the plots have been produced using GNUPLOT [100]. Coordination numbers, radial, and bond angle distribution functions were calculated using the R.I.N.G.S. code [101].

III. RESULTS AND DISCUSSION

A. Properties of TiO₂

First-principles calculations of TiO₂ electronic structure have been discussed extensively in Refs. [102,103]. The calculated PBE0-TC-LRC structural properties and the band gap, using $\alpha = 11.5\%$ and a cutoff of $R_c = 6$ Å, of rutile and anatase are compared with experiments in Table I. For the rutile phase, the lattice parameters are $a = 4.615$ Å, $c = 2.960$ Å, and the band gap is 2.80 eV, which are in good agreement with experiments (4.587 Å, 2.954 Å, 3.03 eV) [104,105]. For anatase TiO₂, the calculated lattice parameters are $a = 3.788$ Å and $c = 9.626$ Å with a band gap of 3.02 eV. These values are also in good agreement with the experimental values of $a = 3.782$ Å, $c = 9.502$ Å, and band gap = 3.2 eV [105,106]. For both TiO₂ phases, the lattice parameters and

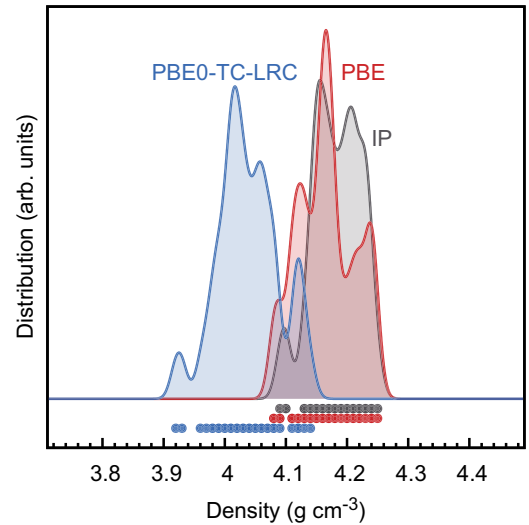


FIG. 1. Density distribution of 50 fully optimized a-TiO₂ structures using interatomic potentials (IPs) and DFT calculations with PBE and PBE0-TC-LRC functionals. A Gaussian smearing of $\sigma = 0.01$ g cm⁻³ was used.

band gaps are reproduced within about 1% and 6%, respectively. We emphasize that the h-DFT functional parameters have been optimized to provide an accurate description of small polaron in a-TiO₂, which is achieved by satisfying the gKc to within 0.08 eV for six different TiO₂ crystalline phases [32].

B. Atomic structure of a-TiO₂

The topology of a-TiO₂ models obtained using classical MD calculations does not change as a result of h-DFT cell and geometry optimization of the structures. The fully optimized PBE0-TC-LRC amorphous structures have an average density of about 4.04 g cm⁻³, ranging from 3.92 to 4.14 g cm⁻³ (see Fig. 1). For the fully optimized IP and DFT a-TiO₂ structures, the average density is 4.18 and 4.16 g cm⁻³, respectively. The density distribution of the amorphous structures is shown in Fig. 1. Experimentally, a-TiO₂ films have a wide range of densities and structural properties depending on preparation methods, as noted, for example, by Bendavid *et al.* [107], where amorphous samples obtained by filtered arc deposition range from 3.62 to 4.09 g cm⁻³ with a change in the substrate bias. To our knowledge, the experimentally reported a-TiO₂ densities range from 3.6 up to 4.4 g cm⁻³ [107–109] whereas calculations have predicted values of 3.68 [43] and 4.18 g cm⁻³ [40]. Similarly, the structures exhibit wide distributions of bond lengths, bond angles, and atomic coordinations compared to the crystalline phases of TiO₂. The coordination number of each atom was determined by counting the number of atoms within a cutoff radius of 2.45 Å. The radial cutoff was chosen at the back of the first peak of the total radial distribution function (RDF) shown in Fig. 2. The Ti ions are five- to seven-coordinated and O ions are two- to four-coordinated. The average abundance (and standard deviation) of five-, six-, and seven-coordinated Ti ions is about 22.78 (5.89), 67.36 (5.26), and 9.89% (3.38%), respectively. For the two-, three-, and four-coordinated O atoms, the average

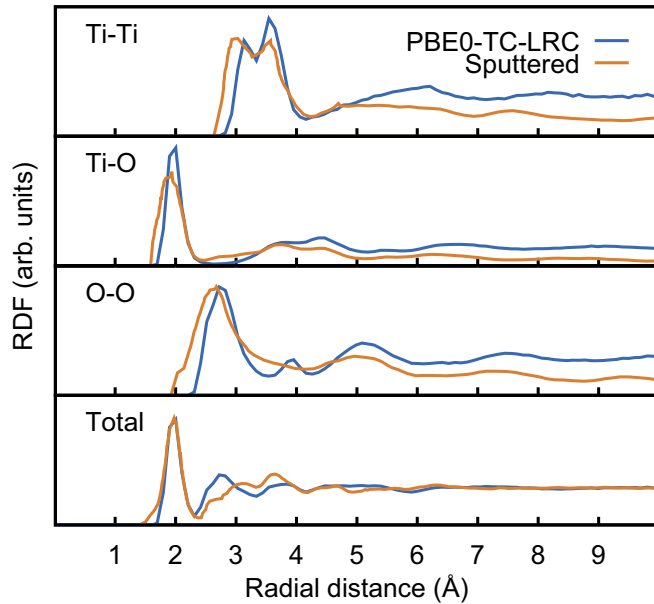


FIG. 2. Average RDF, from 50 structures, of the a-TiO₂ structures fully optimized using the PBE0-TC-LRC functional. Experimental data [7] from sputtered TiO₂ layers is shown in orange as a comparison.

values are 15.36 (3.19), 76.37 (3.02), and 8.28% (2.04%), respectively. We note that in r-TiO₂, Ti atoms are sixfold coordinated and oxygen atoms are threefold coordinated. Figure 3 shows the Ti–O–Ti bond angle distribution, there are two main peaks, with Gaussian-like distribution, at about 100° and 125°, resembling the main Ti–O–Ti angles in the anatase and rutile phase, respectively.

Our calculations also agree with the theoretical results reported previously [39,76] that use the same potential and with the experimental data [7]. The RDF, averaged over the 50 fully optimized PBE0-TC-LRC structures, is shown in Fig. 2. The main sharp pick slightly below 2.0 Å is due to the Ti–O

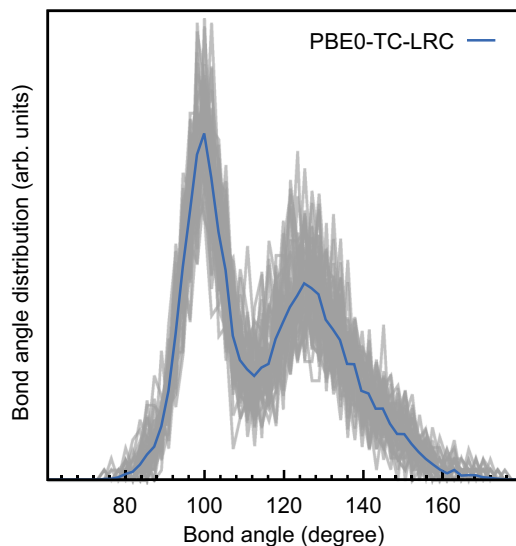


FIG. 3. The Ti–O–Ti bond angle distribution of 50 fully optimized PBE0-TC-LRC a-TiO₂ structures is shown in grey and its average in blue.

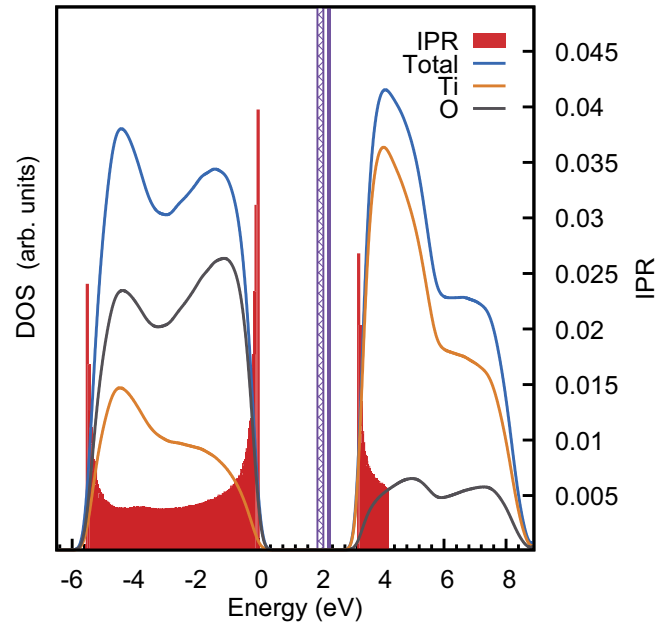


FIG. 4. Average DoS of the a-TiO₂ structures using the PBE0-TC-LRC functional and a Gaussian smearing of 0.15 eV. The IPR values of the one-electron states quantify the charge localization. Large IPR values at the band edges indicate localization of the state and small IPR values indicate delocalization. The mobility edge position can then be estimated from the IPR spectrum. The energy ranges (average plus standard deviation) for the electron (hole) polarons in 50 amorphous structures are shown by solid (hatched) areas in the middle of the band gap. The top of the VB was set to 0.0 eV. The a-TiO₂ DoS and IPR plots were averaged from the 50 different amorphous structures.

bond, whereas the O–O pick is around 2.7 Å. The Ti–Ti main feature is between about 3.0 to 3.8 Å with two main picks in excellent agreement with the experimental observations [7] which have been attributed to edge and corner-sharing octahedra, respectively. The calculated a-TiO₂ RDF is also comparable with those produced using *ab initio* methods [43,64].

C. Electronic structure of a-TiO₂

Figure 4 shows the density of states (DoS) and the IPR spectrum of a-TiO₂ calculated using h-DFT. The a-TiO₂ Kohn-Sham (KS) band gap averaged over 50 a-TiO₂ structures is 3.25 eV, with a standard deviation of 0.10 eV. The valence band (VB) maximum consists mostly of the O 2*p* orbitals and the conduction band edge is derived from Ti 3*d* orbitals. The degree of localization of these states was further analyzed by calculating the IPR spectrum, which has been used to characterise the localization of electronic states in amorphous materials including TiO₂ [41,42] and other (more complex) amorphous structures, see, e.g., Refs. [56,69,110,111]. IPR is calculated for each energy eigenstate of the system and the formulation used here has been reported previously [56]. The average a-TiO₂ IPR spectrum shown in Fig. 4 is similar to those obtained in Refs. [41,42].

The IPR values for electronic states near band edges are higher, indicating that these KS states are more localized. An

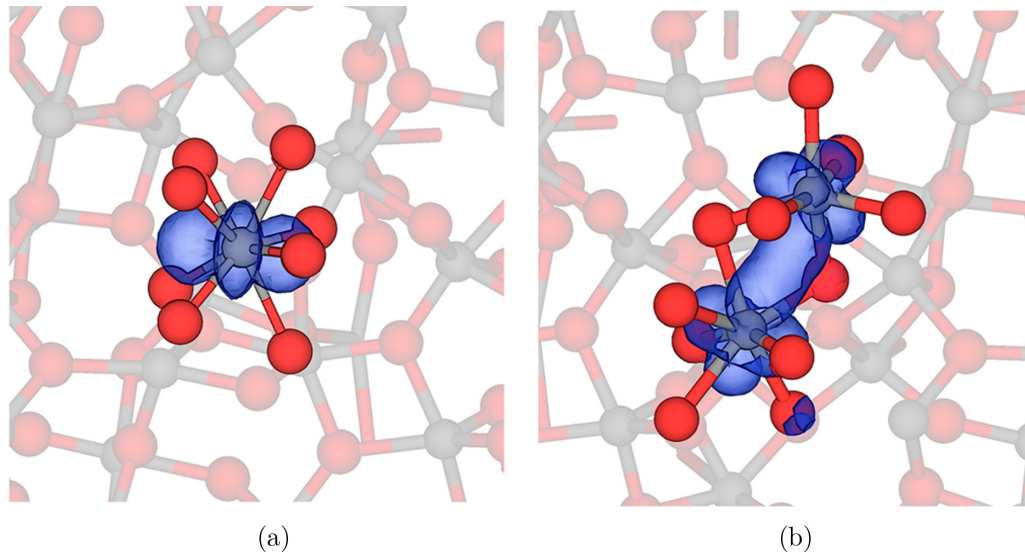


FIG. 5. The spin density of the electron polarons (blue) in a-TiO₂. (a) The electron is localized on a single TiO₈ polyhedra. Ti–O and Ti–Ti distances are increased, on average, by about 0.05 Å. (b) The electron is shared by two adjacent (TiO₇ and TiO₆) polyhedra. Ti–Ti distances are reduced by 0.11 Å, whereas Ti–O distance is increased by 0.03 Å, on average, for both Ti ions holding the electrons. The electron always occupies Ti 3*d* orbitals. Gray and red colors are reserved for Ti and O ions, respectively.

extra electron or hole will tend to occupy these states and structural motifs responsible for these states can be considered as precursor sites for carrier localization. These motifs typically include elongated Ti–O bonds.

D. Electron and hole trapping in a-TiO₂

1. Single electron trapping

To investigate the electron trapping further, an extra electron ($N + 1$, where N is the number of electrons for the neutrally charge structure) was added in 50 amorphous structures. As can be expected from the IPR analysis, initial electron states are not completely delocalized over the entire cell, but rather exhibit localization on few Ti ions. The degree of initial electron localization varies widely across all the samples. Upon the geometry optimization, every structure showed further spontaneous electron localization on Ti 3*d* orbitals. We note that most of the electrons localize on six-coordinated Ti ions, whereas there are a few cases involving seven-coordinated Ti ions and a very small number on eight-coordinated Ti ions [as the one shown in Fig. 5(a)].

Broadly, we can identify two different electron localization types, shown in Fig. 5, which are present in similar concentrations. In the first type [Fig. 5(a)], most of the spin density is localized on a single Ti ion, with Ti–O and Ti–Ti distances increased by about 0.05 Å on average. The latter refers to local distortions close to the localized site (e.g. first-nearest neighbors). For the second type [Fig. 5(b)], the spin density is localized within two corner-sharing Ti polyhedra. In these cases, the extra electron is shared between the two Ti ions [as shown in Fig. 5(b)] with the distance between them reduced by about 0.11 Å, whereas the Ti–O bonds are elongated by 0.03 Å, on average. In the few remaining configurations, the extra electron sits on two or three adjacent Ti ions with no significant spin-density overlap between them.

Trapped electrons create deep KS states in the band gap located at ~ 0.96 eV below the bottom of the conduction band (CB) with a standard deviation of 0.11 eV as indicated by the solid area in Fig. 4 with the width of the area corresponding to the standard deviation of distribution of occupied electron states. This behavior differs from the case of rutile where electron polarons form shallow states on regular Ti sites.

The electron E_T in 50 a-TiO₂ models were calculated as the total energy differences between the initial (partially localized) electron state in the amorphous structure and after the geometry optimization (see Fig. 6). The average E_T is about -0.4 eV with a wide distribution ranging between -0.26 eV and -0.85 eV and a standard deviation of -0.12 eV. The latter corresponds to the standard deviation width of the defect KS state levels created in the band gap by the localized electron, shown in Fig. 4. We note that these E_T are much deeper than those calculated in r-TiO₂ (-0.02 eV) using the same method; no electron localization was predicted for the anatase structure. However, for more accurate determination of E_T and comparison with those in crystal structures, one should use the E_T values calculated with respect to the delocalized states located above the mobility edge. Using the IPR analysis in Fig. 4, one can estimate that the electron mobility edge is located about 0.4 eV deeper in the CB, therefore, E_T should be closer to -0.80 eV for electrons. The large value of E_T suggests stability of localized electrons at room temperature. Moreover, as we show in Fig. 6, the use of the hybrid HSE06 functional does not change our qualitative conclusions. It is well known that there is an underestimation (overestimation) of degree of localization of polaron states in GGA (Hartree–Fock) calculations. Therefore, it is not surprising that the HSE06 functional with $\alpha = 0.25$ produces deeper states than the PBE0-TC-LRC functional with $\alpha = 0.115$.

The IPR analysis (Fig. 4) demonstrates that, on average, there are two or three precursor sites per 270 atoms for an electron to trap. These can be explored either by adding

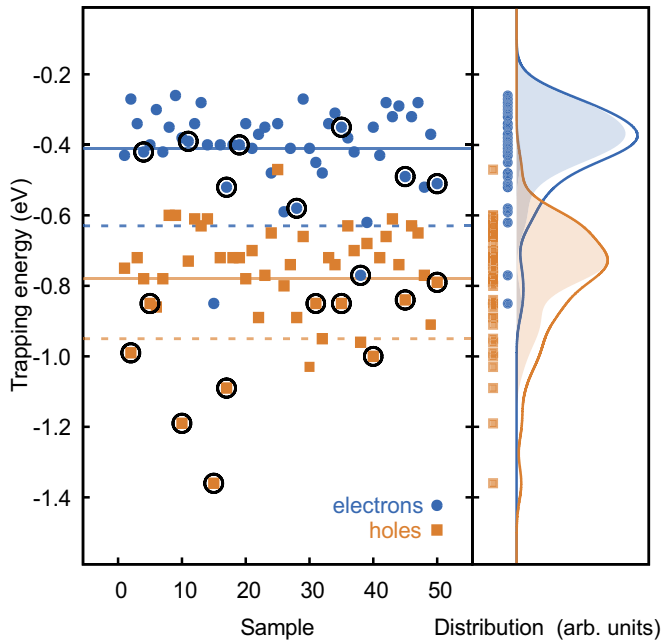


FIG. 6. Calculated E_T for 50 270-atom a-TiO₂ structures using the PBE0-TC-LRC functional with $\alpha = 11.5\%$ and a cutoff of $R_c = 6 \text{ \AA}$. Horizontal lines represent the averages. The dashed horizontal lines show the average taken from ten 270-atom a-TiO₂ structures, using the HSE06 functional. The irreversible cases are shown encircled and the filled curves represent the E_T distribution without these metastable structures. The smeared E_T distribution is shown on the right with a $\sigma = 0.05 \text{ eV}$.

more electrons to the cell or by inducing structural distortion near precursor sites to facilitate the electron localization. In contrast with a-ZnO [56], we could not find a clear correlation between the E_T and the number of Ti ions holding the spin density.

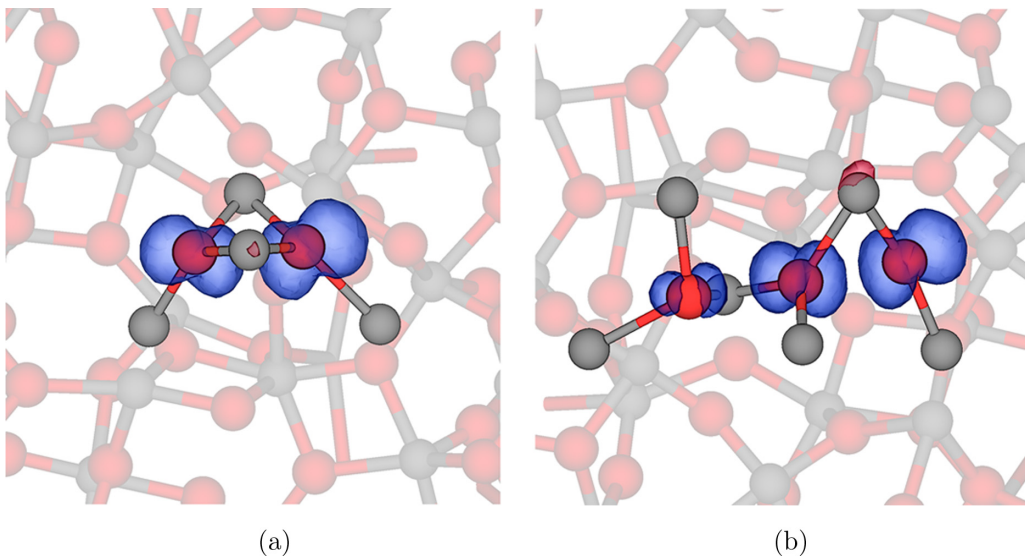


FIG. 7. The spin density of the hole polarons (blue) in a-TiO₂. (a) The hole is shared by two adjacent three-coordinated O ions. O–O distances are 12% shorter than for the neutral case, whereas Ti–O distances are larger by 3.6%, on average. (b) The hole is localized in three adjacent O atoms. On average, Ti–O distances increase by 2.5% and decrease by about 8.8% for O–O distances. The hole always occupies O 2*p* orbitals. Note that the geometry of these features is planarlike in every case.

2. Single hole trapping

Hole localization was studied by removing one electron from the system ($N - 1$). In r-TiO₂, we find no hole trapping but in anatase our calculations predict the hole E_T of $\sim -0.25 \text{ eV}$. The average IPR spectrum in Fig. 4 suggests hole localization in a-TiO₂ with potentially more precursor sites (three to four) than for the electron trapping (two to three).

Every a-TiO₂ structure exhibits hole-trapping states on O 2*p* orbitals. There are two types of localized hole states: in the first one, the hole is localized on two adjacent O ions [Fig. 7(a)], whereas in the second the hole is shared by three O atoms [Fig. 7(b)]. Similar to a-ZnO [56], the geometry of these hole states is planarlike in every structure, as seen in Fig. 7. Among the 50 structures, we did not find one where the hole is localized solely on one O ion. Hole localization causes stronger network distortion than that induced by electrons. One of the reasons for this is that, on average, the states at the top of the VB are more localized than those at the bottom of the CB (see Fig. 4). The Ti–O (O–O) distances are elongated (reduced) after the hole localization by ca. 0.09 Å (0.25 Å) on average.

The unoccupied holes states after the geometry optimization are located approximately 2.0 eV above the top of the VB (1.25 eV below the CB) and a standard deviation of 0.19 eV (see hatched area in Fig. 4). We note that Pham and Wang [39] predicted the hole polaron KS state at $\sim 0.6 \text{ eV}$ above the valence band maximum (VBM), which is outside of the distribution obtained in this work, ranging from 1.51 eV to 2.42 eV in the 50 amorphous structures (see Fig. 4). We believe that this discrepancy is mainly due to the underestimation of the band gap and the different description of charge localization resulting from the DFT+*U* formalism used in Ref. [39] compared to the hybrid exchange correlation functional.

The average hole E_T is -0.78 eV , ranging between -0.37 eV and -1.36 eV . These values are again much

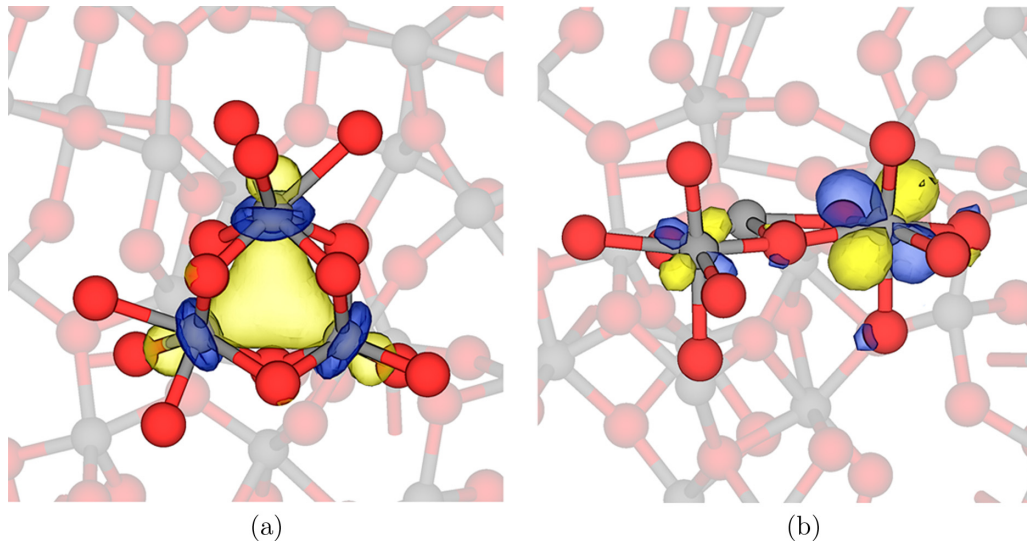


FIG. 8. Localization of two electrons in a-TiO₂. (a) Type (iii), electrons are shared by three adjacent Ti polyhedra. (b) Type (iv), electrons are localized by two Ti ions in a planarlike Ti-O-Ti structure. The colored surfaces correspond to the unoccupied KS states, with blue (yellow) indicating a positive (negative) isovalue. The magnitude of the isovalue was set to 0.05.

deeper than those found for hole trapping in anatase TiO₂ (−0.25 eV). When compared to electron traps in a-TiO₂, E_T hole polarons are about twice as deep. For holes, the estimated mobility edge is about 0.5 eV below the VBM, which would increase the E_T for holes to 1.28 eV, on average. Similar to localized electrons, there is no change in our qualitative results (see Fig. 4) using hybrid HSE06 functional.

3. Reversibility of localized states

As described above, the electron and hole localization causes significant distortions of the surrounding amorphous TiO₂ network. This may cause irreversible changes in model amorphous structures and its relaxation can be part of E_T reported in Fig. 6. When the missing charge is injected back into an amorphous structure, this structure does not always return into its initial state but may transfer into another (lower) minimum of the potential energy landscape. Computationally, this process corresponds to, e.g., photoinduced ionization of trapped states accompanied by relaxation of the neutral structure. This is akin to well-known photoinduced structural changes in amorphous solids particularly well studied in chalcogenides and amorphous H:Si (see, e.g., Refs. [112,113]).

For trapped electrons (holes), we found 9/50 (10/50) structures with a total energy difference between the neutral states before and after charge trapping greater than 0.1 eV and a total energy gain, on average, of 0.26 eV (0.23 eV). This total energy difference may seem small for a 270-atom unit cell. To find out whether the resulting structure is a new local minimum rather than a result of numerical errors, we searched for ionic displacements greater than 0.2 Å in each case. We conclude that in 18 out of 19 cases, a new lower minimum was found. On average, for electron traps, there are eight ions moving by 0.32 Å whereas, for hole traps, there are ten ions that move by 0.30 Å. In some cases, ionic displacement

even stronger ionic displacement than 0.75 Å are induced. The topology of the two local minima is, however, the same. In Fig. 6, we circled the E_T of the “irreversible” structures and the E_T distribution without these metastable “irreversible” cases is shown with filled curves. This distribution which is normal-like without noticeable tails. One can see that the E_T outliers for hole traps correspond to strong network relaxation, leading to transitions into new structures.

E. Electron and hole bipolaronlike states in a-TiO₂

The interaction between localized electrons or holes can lead to formation of more stable systems, often called bipolarons. Hole bipolarons (double holes) have been suggested in many crystalline metal oxides including anatase TiO₂, MoO₃, V₂O₅, InGaZnO, HfO₂, and others [62,63,114,115]. Similarly, the existence of electron bipolarons was predicted in a-SiO₂ [48], where Si–O–Si precursor sites act as deep electron traps and can accommodate up to two extra electrons, and in a-HfO₂ [50]. In this paper, we have investigated the interaction of localized electrons and holes in a-TiO₂ by adding an extra electron (hole) to the existing localized electron (hole) structures in 50 samples. We will call the resulting states bipolarons for brevity in full realization that their stability is caused to a very significant extent by the structural disorder.

In most cases, polarons prefer to stay apart, unless the constituent atoms form bonds or there is a favorable interference of lattice distortions caused by polarons. A measure of the interaction between bipolarons in a crystal is given by its binding energy, E_{bind} , which is defined as

$$E_{\text{bind}} = 2E_{\text{polaron}} - [E_{\text{bipolaron}} + E_{\text{neutral}}], \quad (1)$$

where E_{polaron} ($E_{\text{bipolaron}}$) and E_{neutral} are the charge-corrected energies of the geometry optimized single (double) polaron and neutral periodic cell, respectively. Positive values in-

dicates, therefore, a higher stability for the bipolaron with respect to the two identical infinitely separated polarons. In the amorphous phase, all sites are different and, hence, this expression is approximate. Here we use the energy of the most stable single localized state in each amorphous sample and that obtained after adding the second electron or hole.

1. Interaction between localized electrons in a-TiO₂

As suggested by the IPR analysis and DoS (Fig. 4), extra electrons in a-TiO₂ localize in Ti 3*d* molecular orbitals. Bipolarons are formed either by bonding two Ti ions or in Ti polyhedra sites that can accommodate up to two extra electrons, similar to the structures shown in Fig. 5. Most of the density of the extra electrons is localized on about two to three cations. The average distance between the two cations is 3 Å (with the shortest being ca. 2.75 Å), which corresponds to the shortest distance of the first Ti–Ti nearest neighbors seen in neutral structures (see Fig. 2). When compared to the $N + 1$ cases, there is significant further relaxation on the next-nearest neighbors when the second electron is added.

We can distinguish four structural types of doubly negatively charged structures: (i) The most common is two corner-sharing Ti polyhedra, with two electrons shared mostly between two Ti ions (in ca. 30% of the cases); this interaction leads to the shorter Ti–Ti distances [similar to Fig. 5(b)]. (ii) In about 16% of the structures, the bipolaron is localized mostly on one Ti ion [similar to Fig. 5(a)]. (iii) The bipolaron is delocalized over three Ti ions [Fig. 8(a)]. (iv) In fewer cases, planar Ti–O–Ti connections are formed as illustrated in Fig. 8(b). We observe that in a third of the cases where two electrons are localized on one Ti ion, this is not the same Ti where the first electron was sitting but a different precursor site. In other words, in the process of convergence a different stable site is found. Whether this observation has any significance in terms of bipolaron mobility requires separate investigation.

The distribution of bipolaron binding energies is shown in Fig. 9. In general, two separated electron polarons are more stable than a bipolaron. Only a few structures show a higher stability than two singly charged configurations. The latter is caused by further geometry relaxation due to the electron injection. The energies of bipolaron states [types (i) and (ii), see filled curves in Fig. 9] are distributed across the whole range. The distribution of the binding energies is homogeneous, with energies going from 0.0 eV to -0.5 eV in most cases.

2. Interaction between localized holes in a-TiO₂

As mentioned above, the formation of hole-bipolaron states, which are associated with the formation of peroxidelike O–O bonds, has been reported for anatase TiO₂ and other oxides. For a-TiO₂, we have found that in 12% (one bipolaron for every 2250 atoms) of the structures, there is no energetic barrier to create hole bipolarons [see Fig. 10(a)]. The O–O distance between ions holding the holes is about 1.43–1.45 Å, which agrees with those reported in anatase TiO₂ (1.45–1.49 Å) [62]. We note that the wave function of the unoccupied hole state does not only sit on the the O–O pair but also on neighboring O ions. This reduces the Coulomb

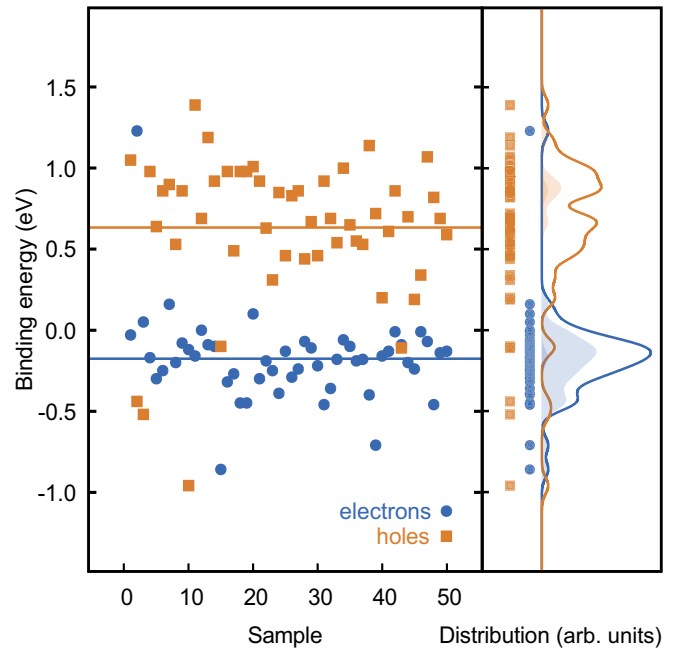


FIG. 9. Calculated binding energies for 50 270-atom a-TiO₂ structures using the PBE0-TC-LRC functional with $\alpha = 11.5\%$ and a cutoff of $R_c = 6$ Å. The filled curves represent the distribution of bipolaron states. The smeared binding energy distribution is shown on the right with a $\sigma = 0.05$ eV.

repulsion between the positive charges facilitating the O–O formation. Hole bipolarons can be formed with O ions of the same Ti polyhedra or through Ti–O–O–Ti connections.

For the remaining configurations, the two holes are localized on adjacent O ions about, on average, 2.47 Å away from each other, forming either linearlike localization as shown in Fig. 10(b) or clustering the localization. Similar to the single hole polarons, the unoccupied KS states are shared by several O atoms. In about 80% of the $N - 2$ structures, the polaron sites differ from those in the $N - 1$ cases, which suggests that creation of new precursor sites can be achieved through small geometry distortions. We also observe that hole bipolarons are significantly more delocalized than two electrons, which is particularly evident in Fig. 10(b).

In contrast to the electron doubly charged structures, hole bipolarons are, in general, more stable than two single polarons, with a binding energies between 0.2 eV to 1.15 eV in most cases. The energies of bipolaron states (see filled curves in Fig. 9) are distributed across the whole range.

IV. SUMMARY AND CONCLUSIONS

To summarize, we studied intrinsic electron and hole trapping in pure amorphous TiO₂ structures. Our results demonstrate that for a-TiO₂, both electrons and holes can be trapped at precursor sites in deep gap states. We have identified these precursor sites by using the IPR spectrum and analysis of trapped states as elongated Ti–O bonds. The electron localization leads to the formation of localized states with energies about 0.96 eV below the bottom of the CB and E_T about -0.4 eV. The hole E_T are even deeper at around

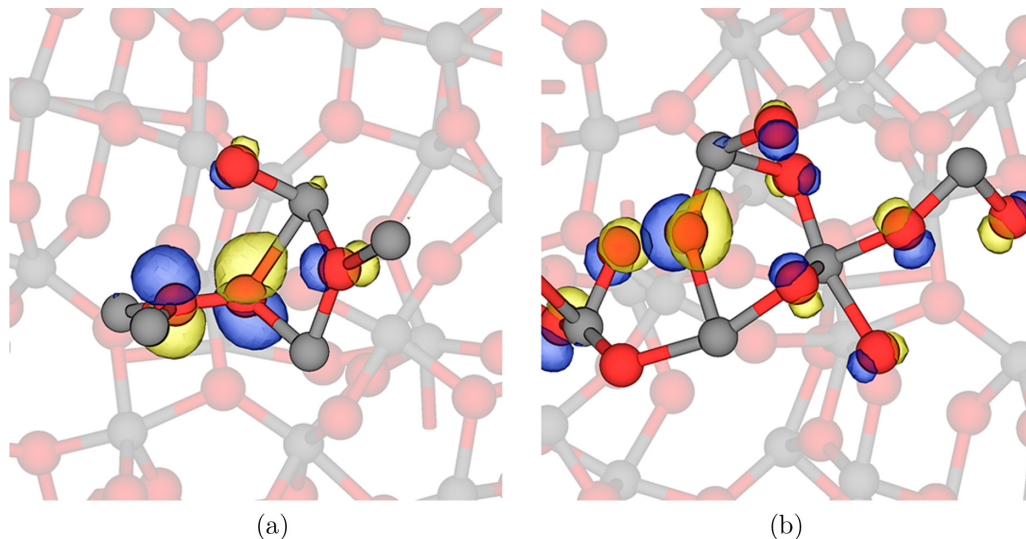


FIG. 10. Localization of two holes in a-TiO₂. (a) Hole bipolaron. (b) Unoccupied KS states are localized on adjacent O ions forming a linearlike localization that runs across the lattice. The magnitude of the isovalue was set to 0.05.

−0.8 eV with localized states at around 2 eV above the top of the VB. With the caveats of the density functional used, the results demonstrate that, similar to other oxides, the electron and hole localization in amorphous TiO₂ creates much deeper states than in crystalline phases. The similar strong electron localization takes place at surfaces and in nanocrystals, where the electrostatic potential and ion coordination near the surface play a crucial role in trapping the extra electrons and holes [29,31,53,116]. However, the local disorder of the amorphous structures amplifies the polaronic relaxation and E_T . Our results demonstrate that a-TiO₂ combines the charge-trapping properties of both rutile and anatase with the electron (hole) E_T at precursor sites being much larger in the amorphous structures. The results can be used for understanding the mechanisms of photocatalysis and improving the performance of electronic and memory devices employing a-TiO₂ films.

One of the main effects of the deep electron and hole trapping at precursor sites in a-TiO₂ is on the carrier mobility. The disordered nature of amorphous materials usually leads to percolative carrier transport with a large characteristic length scale. Accurate simulation of this transport is still a challenging problem for DFT calculations (see, e.g., Ref. [117]) which goes beyond the scope of this paper. Electron transport in a-TiO₂ should involve tunneling between deep

precursor sites and thermal activation into “regular” network sites and hopping between those sites. This may represent an interesting case of crossover from Mott to Efros-Shklovskii variable-range-hopping conductivity discussed in, e.g., Refs. [118,119] for other oxide films.

ACKNOWLEDGMENTS

D.M.-F. and A.L.S. acknowledge funding provided by EPSRC under Grants No. EP/K01739X/1 and No. EP/P013503/1, and by the Leverhulme Trust Grant No. RPG-2016-135. M.K. and A.L.S. are grateful to the World Premier International Research Center Initiative (WPI) sponsored by the Ministry of Education, Culture, Sports, Science and Technology (MEXT), Japan for financial support. Computer facilities on the ARCHER UK National Supercomputing Service have been provided via the UKs HPC Materials Chemistry Consortium (EPSRC Grant No. EP/L000202). This work used the UK Materials and Molecular Modelling Hub for computational resources, which is partially funded by EPSRC (Grant No. EP/P020194). The authors acknowledge the use of the UCL Grace High Performance Computing Facility (Grace@UCL), and the associated support services, in the completion of this work. The authors wish to thank Mohammad Koleini for help in calculations and valuable discussions.

- [1] A. L. Linsebigler, G. Lu, and J. T. Yates Jr, *Chem. Rev.* **95**, 735 (1995).
- [2] M. Pelaez, N. T. Nolan, S. C. Pillai, M. K. Seery, P. Falaras, A. G. Kontos, P. S. Dunlop, J. W. Hamilton, J. A. Byrne, K. O’Shea, M. H. Entezari, and D. D. Dionysiou, *Appl. Catal., B* **125**, 331 (2012).
- [3] J. Schneider, M. Matsuoka, M. Takeuchi, J. Zhang, Y. Horiuchi, M. Anpo, and D. W. Bahnemann, *Chem. Rev.* **114**, 9919 (2014).
- [4] N. Rahimi, R. A. Pax, and E. M. Gray, *Prog. Solid State Chem.* **44**, 86 (2016).
- [5] H. Profijt, S. Potts, M. Van de Sanden, and W. Kessels, *J. Vac. Sci. Technol., A* **29**, 050801 (2011).
- [6] J.-P. Niemelä, G. Marin, and M. Karppinen, *Semicond. Sci. Technol.* **32**, 093005 (2017).
- [7] V. Petkov, G. Holzhüter, U. Tröge, T. Gerber, and B. Himmel, *J. Non-Cryst. Solids* **231**, 17 (1998).
- [8] H. Ennaceri, D. Erfurt, L. Wang, T. Köhler, A. Taleb, A. Khaldoun, A. El Kenz, A. Benyoussef, and A. Ennaoui, *Surf. Coat. Technol.* **298**, 103 (2016).
- [9] S. Hu, M. R. Shaner, J. A. Beardslee, M. Lichterman, B. S. Brunschwig, and N. S. Lewis, *Science* **344**, 1005 (2014).

- [10] H. Y. Jeong, J. Y. Lee, and S.-Y. Choi, *Adv. Funct. Mater.* **20**, 3912 (2010).
- [11] S. Sun, P. Song, J. Cui, and S. Liang, *Catal. Sci. Technol.* **9**, 4198 (2019).
- [12] C. Di Valentin, G. Pacchioni, A. Selloni, S. Livraghi, and E. Giamello, *J. Phys. Chem. B* **109**, 11414 (2005).
- [13] C. Di Valentin, G. Pacchioni, and A. Selloni, *J. Phys. Chem. C* **113**, 20543 (2009).
- [14] M. Setvin, C. Franchini, X. Hao, M. Schmid, A. Janotti, M. Kaltak, C. G. Van de Walle, G. Kresse, and U. Diebold, *Phys. Rev. Lett.* **113**, 086402 (2014).
- [15] V. Bogomolov and D. Mirlin, *Phys. Status Solidi (b)* **27**, 443 (1968).
- [16] C. M. Yim, M. B. Watkins, M. J. Wolf, C. L. Pang, K. Hermansson, and G. Thornton, *Phys. Rev. Lett.* **117**, 116402 (2016).
- [17] N. A. Deskins, R. Rousseau, and M. Dupuis, *J. Phys. Chem. C* **115**, 7562 (2011).
- [18] A. J. Rettie, W. D. Chemelewski, D. Emin, and C. B. Mullins, *J. Phys. Chem. Lett.* **7**, 471 (2016).
- [19] S. Yang, A. T. Brant, N. C. Giles, and L. E. Halliburton, *Phys. Rev. B* **87**, 125201 (2013).
- [20] D. Eagles, *J. Phys. Chem. Solids* **25**, 1243 (1964).
- [21] I. R. Macdonald, R. F. Howe, X. Zhang, and W. Zhou, *J. Photochem. Photobiol., A* **216**, 238 (2010).
- [22] M. Chiesa, M. C. Paganini, S. Livraghi, and E. Giamello, *Phys. Chem. Chem. Phys.* **15**, 9435 (2013).
- [23] I. Austin and N. Mott, *Adv. Phys.* **50**, 757 (2001).
- [24] H. Sezen, M. Buchholz, A. Nefedov, C. Natzeck, S. Heissler, C. Di Valentin, and C. Wöll, *Sci. Rep.* **4**, 3808 (2014).
- [25] P. Deák, B. Aradi, and T. Frauenheim, *Phys. Rev. B* **83**, 155207 (2011).
- [26] P. Deák, B. Aradi, and T. Frauenheim, *Phys. Rev. B* **86**, 195206 (2012).
- [27] P. Zawadzki, K. W. Jacobsen, and J. Rossmeisl, *Chem. Phys. Lett.* **506**, 42 (2011).
- [28] A. Janotti, C. Franchini, J. Varley, G. Kresse, and C. Van de Walle, *Phys. Status Solidi - Rapid Res. Lett.* **7**, 199 (2013).
- [29] M. F. Tabriz, B. Aradi, T. Frauenheim, and P. Deák, *J. Phys.: Condens. Matter* **29**, 394001 (2017).
- [30] C. Spreafico and J. VandeVondele, *Phys. Chem. Chem. Phys.* **16**, 26144 (2014).
- [31] S. Selçuk and A. Selloni, *J. Phys. D* **50**, 273002 (2017).
- [32] A. R. Elmaslmane, M. B. Watkins, and K. P. McKenna, *J. Chem. Theory Comput.* **14**, 3740 (2018).
- [33] B. J. Morgan and G. W. Watson, *Phys. Rev. B* **80**, 233102 (2009).
- [34] N. A. Deskins and M. Dupuis, *Phys. Rev. B* **75**, 195212 (2007).
- [35] S. Lany, *J. Phys.: Condens. Matter* **27**, 283203 (2015).
- [36] M. Reticcioli, U. Diebold, G. Kresse, and C. Franchini, in *Handbook of Materials Modeling*, edited by W. Andreoni and S. Yip (Springer, Cham, 2019).
- [37] S. Yang, A. T. Brant, and L. E. Halliburton, *Phys. Rev. B* **82**, 035209 (2010).
- [38] T. Berger, M. Sterrer, O. Diwald, E. Knözinger, D. Panayotov, T. L. Thompson, and J. T. Yates, *J. Phys. Chem. B* **109**, 6061 (2005).
- [39] H. H. Pham and L.-W. Wang, *Phys. Chem. Chem. Phys.* **17**, 541 (2015).
- [40] N. A. Deskins, J. Du, and P. Rao, *Phys. Chem. Chem. Phys.* **19**, 18671 (2017).
- [41] M. Landmann, T. Köhler, S. Köppen, E. Rauls, T. Frauenheim, and W. G. Schmidt, *Phys. Rev. B* **86**, 064201 (2012).
- [42] B. Prasai, B. Cai, M. K. Underwood, J. P. Lewis, and D. Drabold, *J. Mater. Sci.* **47**, 7515 (2012).
- [43] J. Mavračić, F. C. Mocanu, V. L. Deringer, G. Csányi, and S. R. Elliott, *J. Phys. Chem. Lett.* **9**, 2985 (2018).
- [44] M. H. Rittmann-Frank, C. J. Milne, J. Rittmann, M. Reinhard, T. J. Penfold, and M. Chergui, *Angew. Chem. Int. Ed.* **53**, 5858 (2014).
- [45] K. K. Ghuman and C. V. Singh, *J. Phys. Chem. C* **120**, 27910 (2016).
- [46] J. Strand, M. Kaviani, D. Gao, A.-M. El-Sayed, V. V. Afanas'ev, and A. L. Shluger, *J. Phys.: Condens. Matter* **30**, 233001 (2018).
- [47] A.-M. El-Sayed, M. B. Watkins, V. V. Afanas'ev, and A. L. Shluger, *Phys. Rev. B* **89**, 125201 (2014).
- [48] D. Z. Gao, A.-M. El-Sayed, and A. L. Shluger, *Nanotechnology* **27**, 505207 (2016).
- [49] H.-H. Nahm and Y.-S. Kim, *NPG Asia Mater.* **6**, e143 (2014).
- [50] M. Kaviani, J. Strand, V. V. Afanas'ev, and A. L. Shluger, *Phys. Rev. B* **94**, 020103(R) (2016).
- [51] S. K. Wallace and K. P. McKenna, *Adv. Mater. Inter.* **1** (2014).
- [52] C. Di Valentin and A. Selloni, *J. Phys. Chem. Lett.* **2**, 2223 (2011).
- [53] S. K. Wallace and K. P. McKenna, *J. Phys. Chem. C* **119**, 1913 (2015).
- [54] T. Yamamoto and T. Ohno, *Phys. Chem. Chem. Phys.* **14**, 589 (2012).
- [55] B. J. Morgan and G. W. Watson, *Surf. Sci.* **601**, 5034 (2007).
- [56] D. Mora-Fonz and A. L. Shluger, *Adv. Electron. Mater.* **6**, 1900760 (2020).
- [57] M. H. Cohen, E. N. Economou, and C. M. Soukoulis, *Phys. Rev. B* **29**, 4496 (1984).
- [58] G. Wellein, H. Roder, and H. Fehske, *Phys. Rev. B* **53**, 9666 (1996).
- [59] P. W. Anderson, *Phys. Rev. Lett.* **34**, 953 (1975).
- [60] M. H. Cohen, E. N. Economou, and C. M. Soukoulis, *Phys. Rev. B* **29**, 4500 (1984).
- [61] F. Ambrosio and J. Wiktor, *J. Phys. Chem. Lett.* **10**, 7113 (2019).
- [62] S. Chen and L.-W. Wang, *Phys. Rev. B* **89**, 014109 (2014).
- [63] J. Strand, O. Dicks, M. Kaviani, and A. L. Shluger, *Microelectron. Eng.* **178**, 235 (2017).
- [64] Z. Guo, F. Ambrosio, and A. Pasquarello, *J. Mater. Chem. A* **6**, 11804 (2018).
- [65] Y. Tanaka and M. Suganuma, *J. Sol-Gel Sci. Technol.* **22**, 83 (2001).
- [66] C. Ottermann, R. Kuschnerit, O. Anderson, P. Hess, and K. Bange, *MRS Online Proc. Library Archive* **436**, 251 (1996).
- [67] P. Duwez, R. H. Willens, and W. Klement, *J. Appl. Phys.* **31**, 1136 (1960).
- [68] K. Vollmayr, W. Kob, and K. Binder, *Phys. Rev. B* **54**, 15808 (1996).
- [69] O. A. Dicks and A. L. Shluger, *J. Condens. Matter Phys.* **29**, 314005 (2017).
- [70] D. Mora-Fonz and A. L. Shluger, *Phys. Rev. B* **99**, 014202 (2019).

- [71] E. Olsson, Q. Cai, J. Cottom, R. Jakobsen, and A. L. Shluger, *Comput. Mater. Sci.* **169**, 109119 (2019).
- [72] J. E. Medvedeva, D. B. Buchholz, and R. P. H. Chang, *Adv. Electron. Mater.* **3**, 1700082 (2017).
- [73] M. Matsui and M. Akaogi, *Mol. Simul.* **6**, 239 (1991).
- [74] V. Van Hoang, *Phys. Stat. Sol. B* **244**, 1280 (2007).
- [75] H. H. Pham and L.-W. Wang, *Phys. Chem. Chem. Phys.* **17**, 11908 (2015).
- [76] V. Hoang, H. Zung, and N. H. B. Trong, *Eur. Phys. J. D* **44**, 515 (2007).
- [77] K. K. Ghuman and C. V. Singh, *J. Phys.: Condens. Matter* **25**, 475501 (2013).
- [78] V. Van Hoang, *J. Phys. D: Appl. Phys.* **40**, 7454 (2007).
- [79] G. R. Lumpkin, K. L. Smith, M. G. Blackford, B. S. Thomas, K. R. Whittle, N. A. Marks, and N. J. Zaluzec, *Phys. Rev. B* **77**, 214201 (2008).
- [80] K. Kaur, S. Prakash, N. Goyal, R. Singh, and P. Entel, *J. Non-Cryst. Solids* **357**, 3399 (2011).
- [81] T. Köhler, M. Turowski, H. Ehlers, M. Landmann, D. Ristau, and T. Frauenheim, *J. Phys. D: Appl. Phys.* **46**, 325302 (2013).
- [82] S. Plimpton, *J. Comput. Phys.* **117**, 1 (1995).
- [83] D. Mora-Fonz, J. Christian Schön, J. Prehl, S. M. Woodley, C. R. A. Catlow, A. L. Shluger, and A. A. Sokol, *J. Mater. Chem. A* **8**, 14054 (2020).
- [84] Q. Hou, J. Buckeridge, T. Lazauskas, D. Mora-Fonz, A. A. Sokol, S. M. Woodley, and C. R. A. Catlow, *J. Mater. Chem. C* **6**, 12386 (2018).
- [85] D. Mora-Fonz, T. Lazauskas, M. R. Farrow, C. R. A. Catlow, S. M. Woodley, and A. A. Sokol, *Chem. Mater.* **29**, 5306 (2017).
- [86] J. VandeVondele, M. Krack, F. Mohamed, M. Parrinello, T. Chassaing, and J. Hutter, *Comput. Phys. Commun.* **167**, 103 (2005).
- [87] M. Guidon, J. Hutter, and J. VandeVondele, *J. Chem. Theory Comput.* **5**, 3010 (2009).
- [88] G. Lippert, J. Hutter, and M. Parrinello, *Mol. Phys.* **92**, 477 (1997).
- [89] J. VandeVondele and J. Hutter, *J. Chem. Phys.* **127**, 114105 (2007).
- [90] S. Goedecker, M. Teter, and J. Hutter, *Phys. Rev. B* **54**, 1703 (1996).
- [91] J. P. Perdew, A. Ruzsinszky, G. I. Csonka, O. A. Vydrov, G. E. Scuseria, L. A. Constantin, X. Zhou, and K. Burke, *Phys. Rev. Lett.* **100**, 136406 (2008).
- [92] J. P. Perdew, K. Burke, and M. Ernzerhof, *Phys. Rev. Lett.* **77**, 3865 (1996).
- [93] A. J. Cohen, P. Mori-Sánchez, and W. Yang, *Chem. Rev.* **112**, 289 (2012).
- [94] J. L. Gavartin, P. V. Sushko, and A. L. Shluger, *Phys. Rev. B* **67**, 035108 (2003).
- [95] G. Pacchioni, F. Frigoli, D. Ricci, and J. A. Weil, *Phys. Rev. B* **63**, 054102 (2000).
- [96] J. Lægsgaard and K. Stokbro, *Phys. Rev. Lett.* **86**, 2834 (2001).
- [97] A. V. Krukau, O. A. Vydrov, A. F. Izmaylov, and G. E. Scuseria, *J. Chem. Phys.* **125**, 224106 (2006).
- [98] M. Guidon, J. Hutter, and J. VandeVondele, *J. Chem. Theory Comput.* **6**, 2348 (2010).
- [99] K. Momma and F. Izumi, *J. Appl. Crystallogr.* **44**, 1272 (2011).
- [100] T. Williams, C. Kelley, H.-B. Bröker, J. Campbell, R. Cunningham, D. Denholm, G. Elber, R. Fearick, C. Grammes, and L. Hart *et al.*, Gnuplot 4.6, <http://gnuplot.sourceforge.net/> (2014).
- [101] S. Le Rouxa and P. Jund, *Computational Materials Science* **49**, 70 (2010).
- [102] L. Chiodo, J. M. García-Lastra, A. Iacomino, S. Ossicini, J. Zhao, H. Petek, and A. Rubio, *Phys. Rev. B* **82**, 045207 (2010).
- [103] W. Kang and M. S. Hybertsen, *Phys. Rev. B* **82**, 085203 (2010).
- [104] J. Muscat, V. Swamy, and N. M. Harrison, *Phys. Rev. B* **65**, 224112 (2002).
- [105] D. O. Scanlon, C. W. Dunnill, J. Buckeridge, S. A. Shevlin, A. J. Logsdail, S. M. Woodley, C. R. A. Catlow, M. J. Powell, R. G. Palgrave, I. P. Parkin, G. W. Watson, T. W. Keal, P. Sherwood, A. Walsh, and A. A. Sokol, *Nat. Mater.* **12**, 798 (2013).
- [106] J. K. Burdett, T. Hughbanks, G. J. Miller, J. W. Richardson, and J. V. Smith, *J. Am. Chem. Soc.* **109**, 3639 (1987).
- [107] A. Bendavid, P. Martin, and H. Takikawa, *Thin Solid Films* **360**, 241 (2000).
- [108] M. Fukuhara, H. Yoshida, M. Sato, K. Sugawara, T. Takeuchi, I. Seki, and T. Sueyoshi, *Phys. Status Solidi RRL* **7**, 477 (2013).
- [109] D. Mergel, D. Buschendorf, S. Eggert, R. Grammes, and B. Samset, *Thin Solid Films* **371**, 218 (2000).
- [110] N. Adelstein, C. S. Olson, and V. Lordi, *J. Non-Cryst. Solids* **430**, 9 (2015).
- [111] J. Strand, M. Kaviani, V. V. Afanas'ev, J. G. Lisoni, and A. L. Shluger, *Nanotechnology* **29**, 125703 (2018).
- [112] V. I. Mikla, *J. Phys.: Condens. Matter* **8**, 429 (1996).
- [113] K. Tanaka, *Semiconductors* **32**, 861 (1998).
- [114] A. de Jamblinne de Meux, G. Pourtois, J. Genoe, and P. Heremans, *J. Appl. Phys.* **123**, 161513 (2018).
- [115] H.-H. Nahm, Y.-S. Kim, and D. H. Kim, *Phys. Status Solidi* **249**, 1277 (2012).
- [116] N. A. Deskins, R. Rousseau, and M. Dupuis, *J. Phys. Chem. C* **113**, 14583 (2009).
- [117] A. Massé, P. Friederich, F. Symalla, F. Liu, R. Nitsche, R. Coehoorn, W. Wenzel, and P. A. Bobbert, *Phys. Rev. B* **93**, 195209 (2016).
- [118] R. Rosenbaum, *Phys. Rev. B* **44**, 3599 (1991).
- [119] T. G. Castner, in *Hopping Transport in Solids*, Modern Problems in Condensed Matter Sciences Vol. 28, edited by M. Pollak and B. Shklovski (Elsevier, 1991), pp. 1–47.